Preprint
UCRL-JC-137195

Use of EBSD Data in Numerical Analyses

R. Becker, H. Weiland

This article was submitted to The Minerals, Metals, and Materials Society, St. Louis, MO, October 8-12, 2000

January 14, 2000

U.S. Department of Energy

Lawrence
Livermore
National
Laboratory

USE OF EBSD DATA IN NUMERICAL ANALYSES

Richard Becker[1] and Hasso Weiland[2]

[1] Lawrence Livermore National Laboratory
Livermore, CA 94550
[2] Alcoa Technical Center
Alcoa Center, PA 15069

INTRODUCTION

Experimentation, theory and modeling have all played vital roles in defining what is known about microstructural evolution and the effects of microstructure on material properties. Recently, technology has become an enabling factor, allowing significant advances to be made on several fronts. Experimental evidence of crystallographic slip and the basic theory of crystal plasticity were established in the early 20th century[1-3], and the theory and models evolved incrementally over the next 60 years[4-10]. (Asaro[11] provides a comprehensive review of the mechanisms and basic plasticity models.) During this time modeling was primarily concerned with the average response of polycrystalline aggregates. While some detailed finite element modeling (FEM) with crystal plasticity constitutive relations was done in the early 1980's[12, 13], such simulations over taxed the capabilities of the available computer hardware. Advances in computer capability led to a flurry of activity in finite element modeling in the next 10 years[14-21], increasing understanding of microstructure evolution and pushing the limits of theories and material characterization.

Automated Electron Back Scatter Diffraction (EBSD) has produced a similar revolution in material characterization. The data collected is extensive and many questions about the evolution of microstructure and its role in determining mechanical properties can now be addressed. It is also now possible to obtain sufficient information about lattice orientations on a fine enough scale to allow detailed quantitative comparisons of experiments and newly emerging large scale numerical simulations. The insight gained from the coupling of EBSD and FEM studies will provide impetus for further development of microstructure models and theories of microstructure evolution.

Early studies connecting EBSD data to finite element models used manual measurements to define initial orientations for the simulations[22-24]. In one study, manual measurements of the deformed structure were also obtained for comparison with the model predictions[25]. More recent work has taken advantage of automated data collection on deformed specimens as a means of collecting detailed and spatially correlated data for model validation[26, 27].

Although it will not be discussed in detail here, another area in which EBSD data is having a great impact is on recrystallization modeling. EBSD techniques can be used to collect data for quantitative microstructural analysis[28]. This data can be used to infer growth kinetics of specific orientations, and this information can be synthesized into more accurate grain growth or recrystallization models[29]. Another role which EBSD techniques may play is in determining initial structures for recrystallization models. A realistic starting structure is vital for evaluating the models, and attempts at predicting realistic structures with finite element simulations are not yet successful[30]. As methodologies and equipment resolution continue to improve, it is possible that measured structures will serve as input for recrystallization models. Simulations have already been run using information obtained manually from a TEM[31].

CRYSTAL PLASTICITY MODEL

The impetus behind the growing use of EBSD for characterization and analysis of microstructures is the prominent role that microstructure has in determining many material properties. This implies a corresponding need to include microstructure in material models. To construct models which can capture microstructural effects and which are truly representative of the material at grain level, it is important to incorporate the basic physical mechanisms. For deformation models, this means accounting for changes of shape and lattice orientation based on crystallographic slip.

The ideas of slip and lattice rotation were introduced in Taylor's seminal work[4], and they were given a more complete theoretical treatment in several later papers[7, 11]. The concepts are generally accepted and serve as the basis for polycrystal texture evolution models such as the Taylor model, the Sachs model and self-consistent models. Crystal plasticity constitutive relations have been incorporated into finite element codes for examining details of deformation in single crystals[12-14, 17, 20, 21] and polycrystals[15, 15, 22-25]. Although there are currently many implementations of slip-based models, the basic kinematic description for most existing models is the same.

The integration methods used with early finite element implementations of crystal plasticity relations were developed for stepwise integration of the stress and state variables[12-17]. Some more recent implementations[18, 19, 32-34] follow a total Lagrange formulation where the stress is evaluated directly from a strain energy function and arbitrarily large rigid body rotations can be accommodated within an increment. The kinematics are the same; it is the integration strategy which differs.

Crystal Kinematics

The basis for the kinematic description is a multiplicative decomposition of the deformation gradient, $\mathbf{F}$, into an elastic part, $\mathbf{F}^*$, and a plastic part, $\mathbf{F}^p$.

$$\mathbf{F} = \mathbf{F}^* \cdot \mathbf{F}^p \,. \tag{1}$$

This is shown schematically in Figure 1. The plastic part captures the deformation by crystallographic slip. It does not distort the lattice or change its orientation. The elastic part accounts for rotation and distortion of the crystal lattice.

The plastic deformation within a volume element is specified in terms of the average slip rate, $\dot{\gamma}^\alpha$, on a slip system. The slip rate is related to the plastic part of the deformation gradient by

$$\dot{\mathbf{F}}^p \cdot \mathbf{F}^{p\,-1} = \sum_{\alpha=1}^{N} \dot{\gamma}^\alpha \, \mathbf{s}_0^\alpha \otimes \mathbf{m}_0^\alpha \,, \tag{2}$$

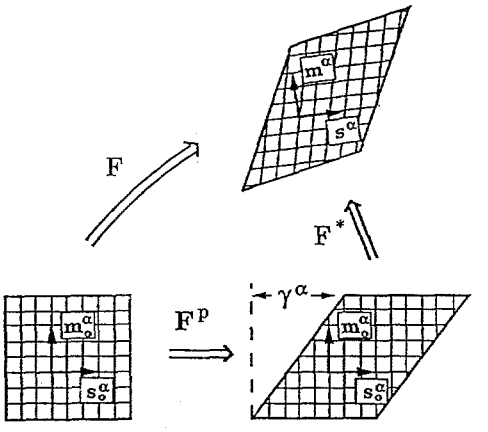

Figure 1. Illustration of deformation by slip and distortion of the crystal lattice.

where the slip plane normal is given by $\mathbf{m}_0^\alpha$ and the slip direction is $\mathbf{s}_0^\alpha$. The superscript α is an index representing one of N slip systems. Equation (2) is a representation of the deformation rate in the intermediate configuration of Figure 1 where the lattice is undistorted and in its initial orientation.

An expression giving the slip rate in the current configuration can be found by constructing the velocity gradient, $\mathbf{L}$, from Eq. (1)

$$\frac{\partial \dot{x}}{\partial x} = \mathbf{L} = \dot{\mathbf{F}} \cdot \mathbf{F}^{-1} = \dot{\mathbf{F}}^* \cdot \mathbf{F}^{*-1} + \mathbf{F}^* \cdot \dot{\mathbf{F}}^p \cdot \mathbf{F}^{p-1} \cdot \mathbf{F}^{*-1} . \tag{3}$$

The first and second terms on the right hand side are the elastic and plastic parts of the velocity gradient, $\mathbf{L}^*$ and $\mathbf{L}^p$, respectively. Using Eq (2), the plastic part of the velocity gradient can be written as

$$\mathbf{L}^p = \sum_{\alpha=1}^{N} \dot{\gamma}^\alpha \mathbf{s}^\alpha \otimes \mathbf{m}^\alpha \tag{4}$$

where

$$\mathbf{s}^\alpha = \mathbf{F}^* \cdot \mathbf{s}_0^\alpha \qquad \text{and} \qquad \mathbf{m}^\alpha = \mathbf{m}_0^\alpha \cdot \mathbf{F}^{*-1} \tag{5}$$

are the slip direction and slip plane normal in the current configuration. $\mathbf{s}^\alpha$ and $\mathbf{m}^\alpha$ are assumed to be orthogonal for slip processes, so the plastic part of the deformation is isochoric.

Equations can be written for the evolution of $\mathbf{s}^\alpha$ and $\mathbf{m}^\alpha$ in terms of $\dot{\mathbf{F}}^*$ by taking time derivative of Eq. (5). However, in practice they are typically evaluated directly from Eq. (5) for a given $\mathbf{F}^*$. $\mathbf{F}^*$ is either integrated from

$$\dot{\mathbf{F}}^* = (\mathbf{L} - \mathbf{L}^p) \cdot \mathbf{F}^* , \tag{6}$$

or it is calculated through Eq. (1) where $\mathbf{F}$ is known from the configuration and $\mathbf{F}^p$ is integrated from Eq. (2)

$$\dot{\mathbf{F}}^p = \left(\sum_{\alpha=1}^{N} \dot{\gamma}^\alpha \mathbf{s}_0^\alpha \otimes \mathbf{m}_0^\alpha \right) \cdot \mathbf{F}^p . \tag{7}$$

Integration through Eq. (6) is used with updated Lagrangian methods while Eq. (7) combined with Eq. (1) is often used in full Lagrangian formulations.

Stress Strain Relations

It is assumed that the stress is related to the elastic distortion of the crystal lattice through a strain energy function ϕ. In particular, the second Piola-Kirchhoff stress tensor, $\mathbf{T}^*$, and its rate can be given by

$$\mathbf{T}^* = \frac{\partial \phi}{\partial \mathbf{E}^*} \qquad \text{and} \qquad \dot{\mathbf{T}}^* = \frac{\partial^2 \phi}{\partial \mathbf{E}^{*2}} : \dot{\mathbf{E}}^* = \mathcal{C} : \dot{\mathbf{E}}^* \tag{8}$$

The Lagrangian strain of the lattice, $\mathbf{E}^*$, is

$$\mathbf{E}^* = \frac{1}{2}\left(\mathbf{C}^* - \mathbf{I}\right); \qquad \mathbf{C}^* = \mathbf{F}^{*T} \cdot \mathbf{F}^* \tag{9}$$

where $\mathbf{C}^*$ is the right Cauchy-Green stretch tensor of the lattice. $\mathcal{C}$ in Eq. (8b) is the forth order crystal modulus tensor, usually set in a reference frame coincident with principle lattice directions.

The second Piola-Kirchhoff stress is related to the Kirchhoff stress, $\boldsymbol{\tau}$, and the Cauchy stress, $\boldsymbol{\sigma}$ as

$$J\boldsymbol{\sigma} = \boldsymbol{\tau} = \mathbf{F}^* \cdot \mathbf{T}^* \cdot \mathbf{F}^{*T} \tag{10}$$

where $J = \det(\mathbf{F})$, is the ratio of the deformed volume to the reference volume. Since the plastic deformation is isochoric, $J = \det(\mathbf{F}^*)$, the elastic volume change. It is typically very close to one for industrial forming operations, so the distinction between Cauchy stress and the Kirchhoff stress is usually ignored.

An expression for the stress rate can be obtained by taking the derivative of Eq. (10) and combining terms[11, 12]. After some manipulation, the Jaumann rate of the Kirchhoff stress can be written as

$$\overset{\nabla}{\boldsymbol{\tau}} = \dot{\boldsymbol{\tau}} - \boldsymbol{\omega}\cdot\boldsymbol{\tau} + \boldsymbol{\tau}\cdot\boldsymbol{\omega} = \mathcal{K} : \mathbf{D} - \sum_{\alpha=1}^{N} \dot{\gamma}^\alpha \mathbf{R}^\alpha \tag{11}$$

where $\mathbf{D}$ is the rate of deformation tensor (symmetric part of the velocity gradient, $\mathbf{L}$); $\boldsymbol{\omega}$ is the spin tensor (asymmetric part of the velocity gradient, $\mathbf{L}$); $\mathcal{K}$ is a fourth order modulus obtained by rotating the crystal modulus $\mathcal{C}$ into the laboratory reference frame and adding a few terms on the order of stress; $\mathbf{R}^\alpha$ is given by

$$\mathbf{R}^\alpha = \mathcal{K} : \mathbf{P}^\alpha + \mathbf{W}^\alpha \cdot \boldsymbol{\tau} - \boldsymbol{\tau} \cdot \mathbf{W}^\alpha \tag{12}$$

and

$$\mathbf{P}^\alpha = \frac{1}{2}\left[\mathbf{s}^\alpha \otimes \mathbf{m}^\alpha + \mathbf{m}^\alpha \otimes \mathbf{s}^\alpha\right] \qquad \text{and} \qquad \mathbf{W}^\alpha = \frac{1}{2}\left[\mathbf{s}^\alpha \otimes \mathbf{m}^\alpha - \mathbf{m}^\alpha \otimes \mathbf{s}^\alpha\right] \tag{13}$$

Equation (11) is used in updated Lagrangian integration schemes where the stress is integrated in time. Equation (8a) is often used to compute the stress directly from $\mathbf{E}^*$ in full Lagrangian formulations. Although the relations for the full Lagrangian approach appear much simpler, the derivatives needed for a Newton iteration scheme resemble Eqs (11) and (12). Actual coding for the full Lagrangian formulation can be somewhat more involved because of convergence checking and correction updates. The advantage of the full Lagrange formulation is stability and accuracy for large rigid body rotation increments.

Slip System Constitutive Relations

For crystals obeying the Schmid criterion, slip is assumed to be related only to the resolved shear stress on the slip systems. In a rate independent model, the slip rate is generally

taken to be proportional to the rate of change of the resolved shear stress. In a rate dependent model, the slip rate is assumed to be related to the resolved shear stress itself, not its rate. The resolved shear stress on a slip system, τ^α, can be determined from

$$\tau^\alpha = \mathbf{m}_0^\alpha \cdot \mathbf{T}^* \cdot \mathbf{C}^* \cdot \mathbf{s}_0^\alpha \tag{14}$$

in the intermediate configuration of Figure 1, and

$$\tau^\alpha = \mathbf{m}^\alpha \cdot \boldsymbol{\tau} \cdot \mathbf{s}^\alpha \tag{15}$$

for a formulation based in the current configuration.

Because slip on multiple combinations of slip systems can accommodate many deformation modes, rate independent constitutive models can lead to ambiguities in the solution. The degree of slip on each system may be indeterminate. Although use of some slip system hardening relations[35] or the single valued decomposition method[36] can be used to obtain a solution, the most common method currently employed to circumvent this slip system indeterminacy is to use a rate dependent slip system model. Here the slip rate is given uniquely in terms of the resolved shear stress on the slip system, τ^α, and its resistance to slip, g^α.

A simple power law strain rate sensitivity takes the form:

$$\dot{\gamma}^\alpha = a \, \mathrm{sign}(\tau^\alpha) \left(\left| \frac{\tau^\alpha}{g^\alpha} \right| \right)^{1/m} \tag{16}$$

where a is a reference slip rate and m is the strain rate sensitivity exponent.

The resistance of a slip system can written as an evolution equation

$$\dot{g}^\alpha = \sum_{\beta=1}^{N} H_{\alpha\beta} \, \dot{\gamma}^\beta \tag{17}$$

where $H_{\alpha\beta}$ is an evolving matrix capturing hardening interactions among slip systems. The model allows considerable flexibility for specifying the strength evolution, but most current simulations adopt a rather simple specification where $H_{\alpha\beta}$ evolves proportionally with deformation:

$$H_{\alpha\beta} = g' \, h_{\alpha\beta} \tag{18}$$

Here, g' is a function of the accumulated slip and $h_{\alpha\beta}$ is a constant matrix. If the hardening of a slip system due to its own activity is assumed to be equal to the hardening of the system due to activity on other slip systems, $h_{\alpha\beta}$ is fully populated with ones. This is the most common assumption, and it was the assumption used in generating the results presented here. More comprehensive slip system hardening models have been proposed which more accurately represent detailed observations of secondary slip initiation[37,38], but these have not yet found widespread use in modeling activities.

CRSYTAL MODEL VALIDATION

As the automated collection of EBSD data is relatively new, methods of coupling the experimental data to finite element simulations are still under development. While there have been several excursions into applications[23,24], most EBSD-FEM studies to date have been conducted for purposes of model validation. Some earlier studies used manually collected measurements of orientations on a section before and after deformation to assess the validity

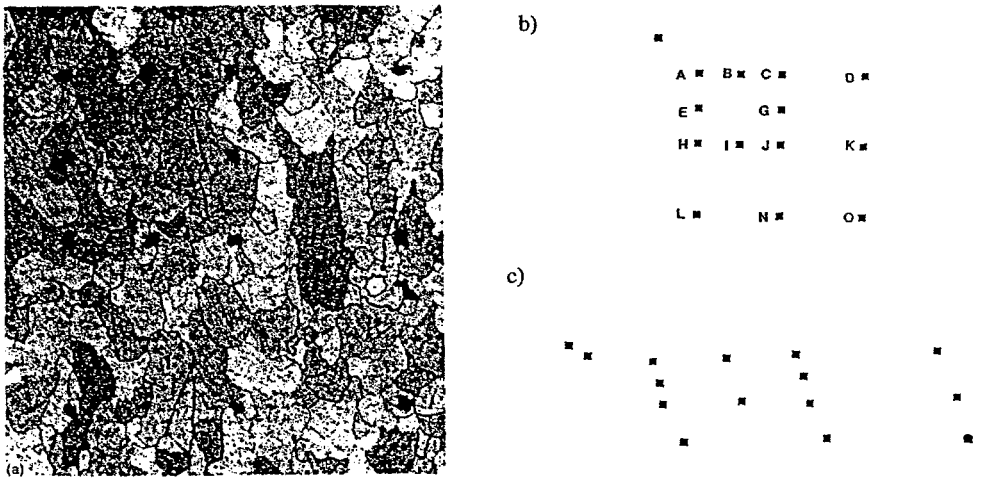

Figure 2. Microhardness indents on the split channel die compression specimen: a) as seen on the specimen; b) initial indent pattern and c) pattern after deformation.

of FEM solutions[25]. More recent efforts are using automatically collected data and three dimensional deformation models[26, 27].

Split Channel Die Polycrystal Sample

An early validation study using EBSD data was conducted by Panchanadeeswaran, et al[25, 39]. They took an as cast, commercial purity aluminum sample with a 200 μm grain size and machined it for a channel die compression experiment. The sample was split in half with the dividing plane normal being in the constraint direction of the specimen. Both new surfaces were polished. One of the mating surfaces had a region marked with microhardness indents over a 2 × 2 mm square area. The grain morphology and orientations in the region were then recorded, Figure 2a,b. The sample was reassembled and deformed to 40% reduction in the channel die at 375°C.

The locations of the hardness indents were recorded from the deformed sample and used to calculate the average strain experienced by the region. There was substantial shear in addition to the compression, as evident in Figure 2c. This shear is consistent with the inadvertent macroscopic shear of the specimen during the compression test. Manual orientation measurements were made on several grains in the marked area of the deformed sample.

The measured locations of the initial grain boundaries from a region containing 35 grains were used to construct a two dimensional finite element mesh of 2187 quadrilateral elements in which the mesh lines conformed to the grain boundaries. The mesh was continuous across the grain boundaries, simulating deformation with no grain boundary sliding. The initial lattice orientations for each grain were assigned based on the measurements.

The slip system hardening and strain rate sensitivity used in the simulation were deduced by taking polycrystal data and using an average Taylor factor to scale the stress and strain rate to obtain approximate values of resolved shear stress and slip rate. All slip systems were assumed to harden equally. With this construction, a Taylor polycrystal model will approximately replicate the original experimental stress strain curve. The two dimensional model was deformed in plane strain compression with the final applied deformation being consistent with that measured from the microhardness indents, Figure 2c.

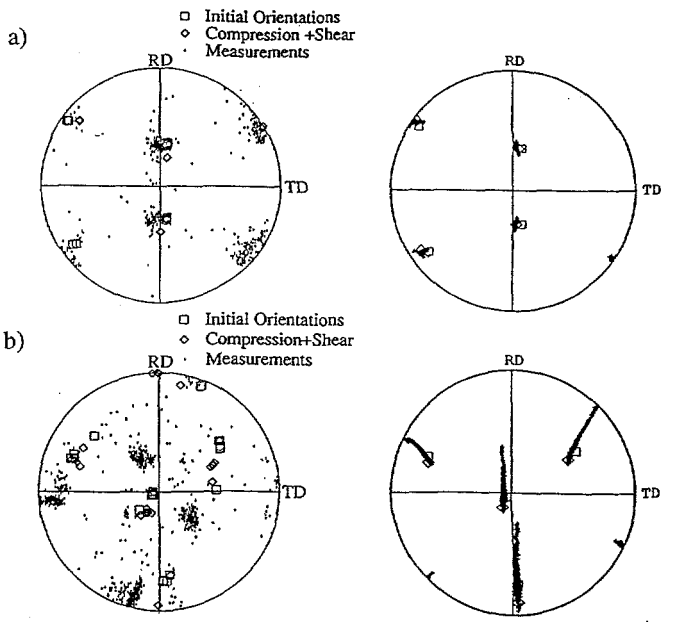

Figure 3. Comparison of experimental and predicted (111) pole figures from the split channel die compression study. Examples of a) agreement and b) disagreement. Experimental pole figures are on the left and the model results are on the right.

Comparison of the experimental and calculated orientation distributions for individual grains shows some in which agreement is good, Figure 3a and others where the simulations failed to predict the observed orientation spread, Figure 3b. In general, agreement was only found when orientation changes were small. Since such grains do not provide a critical test for the model, one might be hesitant to conclude that the model predictions were proven successful for any of the grains examined.

Observation of many pole figures from the simulation showed that orientation changes resulted primarily from rotations about an axis normal to the model plane. This was the case even though all twelve slip systems were modeled and the lattice was free to rotate about any arbitrary axis in three dimensional space. Rotation only about the model plane was also observed in an earlier study[22]. This behavior is thought to be a result of the kinematic freedom for material spin about that axis and only capturing shear stress and grain interactions in the model plane. Using the same initial configuration and 90 degree rotated initial orientations in a generalized plane strain model, where the compression is in the out of plane direction, the coincidence of the rotation axis with the model plane was again evident[25]. This verified that the predominant rotation about the model plane is indeed an artifact of the two-dimensional model. In addition to these difficulties, it was clear from the results that grain shapes and the influence of neighboring grains have a significant impact on orientation changes. Thus, it is important to include the grain structure in all directions.

A conclusion from the study was that it is not possible to obtain a realistic approximation of a deformed three dimensional microstructure with a two dimensional model except for a very restricted class of orientations. Accurate predictions of local lattice orientations require a detailed three dimensional representation of the microstructure and a means of applying boundary conditions to the model without introducing significant artificial constraint.

These conclusions suggest two paths for constructing model validation studies: characterize and test a three dimensional grain structure or construct idealized specimens for which the grain structure is known. With current technology, the former option involves serial sectioning where the specimen is destroyed. This prohibits one to one validation, but it is useful for deformation studies on a larger size scale. Such characterization has been performed on a tantalum specimen[40]. The second validation option is achievable by constructing columnar grain samples where the grain structure is constant in one direction. While the configuration is not representative of a typical polycrystal sample, it is useful for model validation.

Deformation of a Quasi-Columnar Grain Sample Along the Growth Direction

Two recent studies have used columnar grain samples in coordinated EBSD-FEM validation efforts. Both studies started with the same directionally solidified aluminum castings which produced quasi-columnar grains running in the solidification direction. Nearly all of the grains had a (001) crystal direction approximately aligned with the solidification direction. In the work by Bhattacharyya, et al[27], a 3 mm thick slice of the casting was examined where the columnar axis was in the thickness direction of the slice. The sample was characterized by EBSD on both sides of the slice. Since the columnar grain growth was imperfect, there was a variation in grain shape from one side to the other. One side had coarser grains, indicating that some of the grains terminated within the specimen. The sample was compressed 40% of its initial height by uniaxial compression with the compression axis being the axis of the columnar grains. Since the initial orientations were near (001) and the stable orientation for uniaxial compression is (110), considerable lattice rotation was expected.

The deformed specimen was characterized by automated EBSD for comparison with the simulations. A prominent feature found on the orientation maps was the occurrence of distinct bands or regions of differing orientation within the grains. In some grains the bands were solitary, while in others, several narrow parallel bands of alternating orientation were observed.

A uniform finite element mesh of hexahedral elements was created to model the compression specimen. Mesh regions were identified with specific grains from the initial IOM map of the coarse grained side of the sample, and the appropriate orientations were assigned to the elements. Since the mesh was regular, the mesh lines did not conform to the grain boundaries, and the grain boundaries in the model had a stepped appearance. The specimen was modeled with one element through the thickness of the slice. Boundary conditions applied to the four planes orthogonal to the compression plane required that these faces remain planar and orthogonal.

An orientation map constructed from the deformed finite element model failed to show the orientation banding observed in the experiments, and comparison of the predicted pole figures with the experimental results also failed to show the correct distribution of lattice rotation in many grains. These two observations are consistent and suggest that the local deformation pattern may not have been predicted correctly either. Since deformation is a combination of rotation and strain, this lack of agreement in orientation also suggests that the deformation pattern may be in error. Potential reasons for failure of the model will be discussed below.

Transverse Deformation of a Quasi-Columnar Grain Sample

In another study[26] using the columnar grain material, segments of the casting were annealed prior to excising the specimens. This produced centimeter sized grains with considerably less variation along the growth axis. Channel die compression specimens with

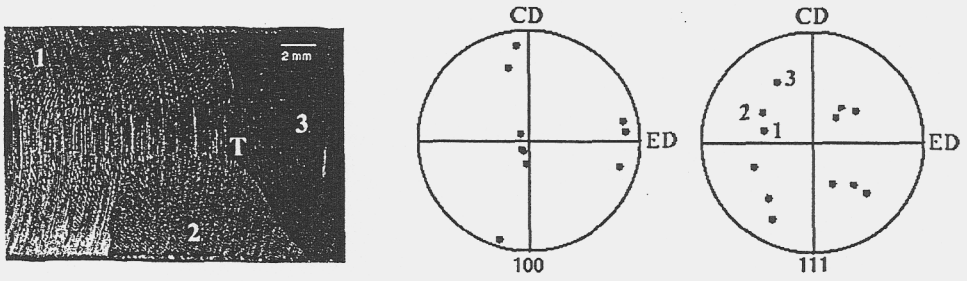

Figure 4. Initial specimen geometry and orientation for columnar grain tricrystal.

dimensions 10 mm thick by 15 mm high by 25 mm long were then machined for this study. The growth axis of the grains was aligned with the constraint direction (10 mm direction) of the channel die. The grain patterns were very similar on both sides of the specimen, indicating that the desired columnar grain structure was nearly achieved. The initial grain structure was photographed on all faces, and the grain orientations were measured at several points by EBSD. As with the study described above, the grains tended to have the (001) direction aligned within 5 to 10 degrees of the growth axis. The samples were deformed to 15% compression in a channel die at room temperature and at 200°C.

Here, attention will be focused on one sample which contained three grains. The specimen and its initial lattice orientations are shown in Figure 4. The deformed specimen is shown in Figure 5. As the sample was deformed in a channel die, little deformation occurred in the out of plane direction. However, deformation by slip has normal-shear coupling, and the deformation on the plane normal to the constraint direction varied through the thickness of the sample. For example, the "foot" on the lower right of the deformed sample varied in size and shape through the thickness of the specimen.

OIM scans of the deformed sample were taken from within the three boxes indicated on Figure 5. Two of these are within single crystal regions fairly far removed from a grain boundary and the third, the center box, includes all three grains near the triple point. Orientation maps from these three regions and the corresponding (111) pole figures are shown in Figures 6-8. The contour maps in Figures 6 and 7 were created by selecting a location near the center of the region and applying the same shading to all points which had an orientation within 5° of the selected orientation. Regions with an orientation greater than 5 degrees from the reference were shaded another color. The same shading is applied to the corresponding points on the pole figures. The white lines on the contour plots represent the orientations of slip traces observed on the surface of the deformed specimen.

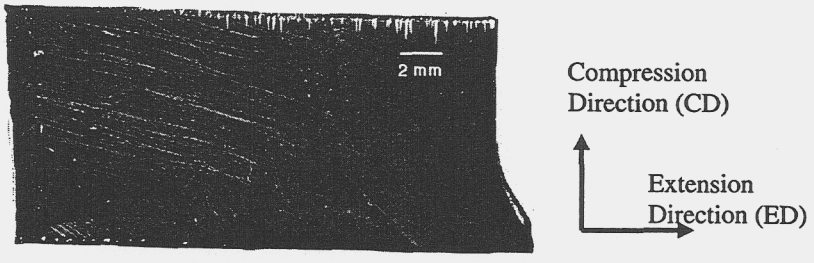

Figure 5. Columnar grain tricrystal following 14% compression in a channel die. The white rectangles mark regions where OIM scans were taken.

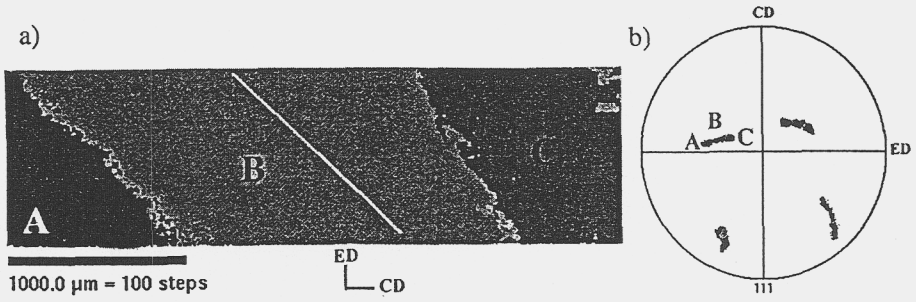

Figure 6. OIM orientation map from the rectangular region in grain #1 of Figure 5. The white line indicates the slip trace direction.

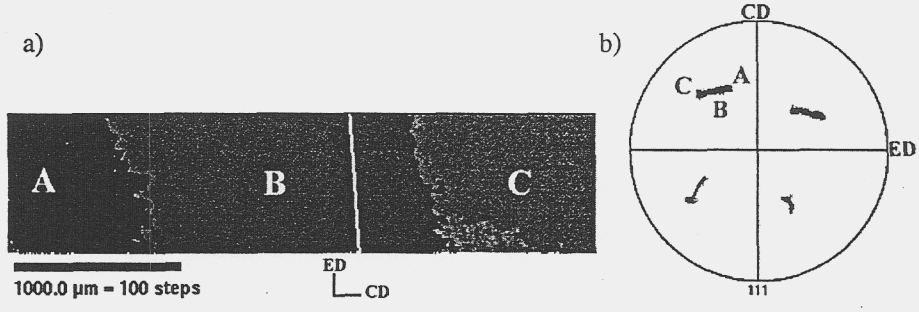

Figure 7. OIM orientation map from the rectangular region in grain #3 of Figure 5. The white line indicates the slip trace direction.

Figures 6 and 7 are, respectively, from the large single crystal regions on the left and right ends of the specimen. In both cases, the lattice rotation from one end of the plot to the other is greater than 10 degrees. The contour boundaries are aligned with the slip traces in both cases. This suggests that the orientation is roughly constant along the slip trace and that the orientation gradient is greatest in the direction normal to the slip plane. Had slip occurred uniformly in the region, the lattice would have the same orientation throughout. Hence, the plots indicate a significant gradient in slip activity over the region.

The OIM scan containing the triple point, Figure 8, is more complex, but the same correlation can be observed between the orientation gradients and the dominant slip trace: the orientation is fairly constant along the direction of the slip trace, and it varies normal to the trace. It is also observed that the slip traces lie along different directions than in the regions of the crystal remote from the triple junction. This is a result of the complex stress state found at the triple point. Grain 3 in Figure 8 also displays a banded orientation structure reminiscent of that observed by Bhattacharyya et al[27]. The lack of such a structure in other portions of the same grain, Figure 7, supports the hypothesis that such structures form for certain combinations of loading and crystal orientations and not others.

The finite element mesh used to simulate the deformation is shown in Figure 9. It contains approximately 20000 hexahedral elements. The lattice orientations were assigned based on the EBSD measurements. Boundary conditions were chosen to simulate deformation in a channel die. The width of the channel was wider than the undeformed specimen to permit insertion of the specimen along with PTFE tape for a lubricant. To capture the initial broadening of the specimen, the channel was modeled as rigid surfaces 10.35mm apart while

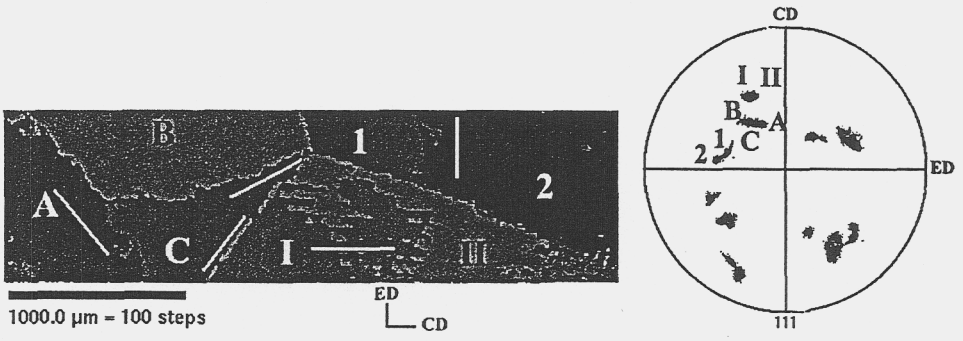

Figure 8. OIM orientation map covering the triple junction of the tricrystal. Regions labeled 1 and 2 are subdivisions of grain #1; A, B and C are subdivisions of grain #2; and I and II are subdivisions of grain #3. The white line indicates the slip trace direction.

the initial specimen width was 9.98mm. This allows a lateral spread of approximately 4%. Deformation was achieved by displacing the upper surface with respect to the lower at a constant velocity.

The deformed specimen shape and predicted contours of accumulated slip are shown in Figure 10. The specimen outline shows that a "foot" was predicted on the lower left of the specimen, but the magnitude and shape differ from that observed in Figure 5. Another feature of the deformed shape worth noting is the slope of the boundary on the left side of the crystal. The simulation predicts that the boundary will be inclined with the top moving toward the right with respect to the bottom. The experiment shows the top moving toward the left with respect to the bottom. This is obviously a source of concern. In attempts to obtain better qualitative agreement, many perturbations were made to the initial orientation, the friction, slip system hardening relations, strain rate sensitivity and channel width. None of these measures caused the slope on the left side of the model to have the correct sign.

The predicted pole figure from the model region corresponding to Figure 6 shows no discernible orientation spread and very little lattice rotation. This is consistent with Figure 10 which shows little difference in accumulated slip across the region.

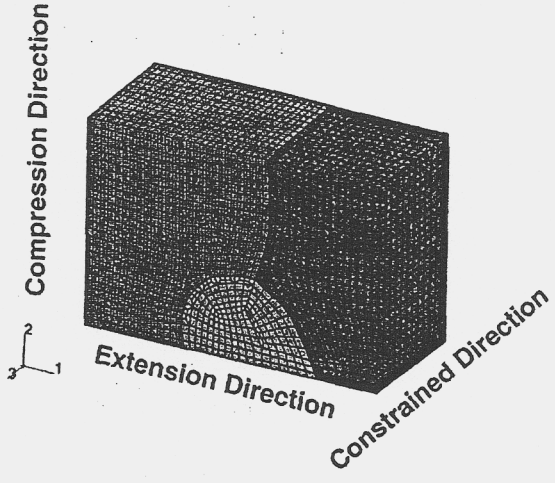

Figure 9. Finite element mesh used to simulate the deformation of the columnar grain tricrystal.

Figure 10. Predicted contours of accumulated slip from the finite element model of the tricrystal.

Direct Mapping of IOM Data to a Finite Element Simulation

In the examples cited above, regions of the finite element model were defined as grains based on grain boundaries identified through micrographs or IOM data. All of the elements within each grain were assigned the same initial orientation. A more direct and automated assignment of orientations was explored by Kallivayalil, et al[41]. In that work, a region near the surface of an aluminum sample was characterized by an automated IOM scan. A 100 $\times$ 250 regular finite element mesh was constructed to be the same size as the scanned region. The initial lattice orientation of each element was determined by calculating the element centroid coordinates and locating the nearest corresponding point in the OIM map. This orientation was assigned to the element. As a result of this initialization procedure, any orientation variation present in the measurements was reflected in the finite element model. A contour plot of R_{11}, a component of the rotation matrix identifying the initial orientation of the crystal lattice, is shown in Figure 11. The plot looks remarkably like an OIM orientation map.

The free surface of the specimen is at the bottom of the model shown in Figure 11. The nodes on the upper surface were constrained from motion in the vertical direction but were free to move horizontally. On the left side of the model, the nodes were constrained horizontally and free to move vertically. Deformation was applied by moving the nodes on the right side of the model. The region was deformed 4% in plane strain tension.

Contours of accumulated slip from the simulation are shown in Figure 12. The notable feature of these results is the appearance of fine structure and slip patterning. These features appear realistic but have not been observed in other simulations. They could be the result of a combination of factors, but further exploration is needed to determine a definite origin. The most obvious factors distinguishing this model from others are: a) a very fine spatial discretization giving the solution significantly more degrees of freedom, b) a large number of grains and interacting neighbors to drive nonuniform deformation patterns, and c) the presence of a free surface on the bottom of the model.

CRYSTAL MODEL VALIDATION

The availability of data collected from automated EBSD enables a critical evaluation of the accuracy of meso scale finite element crystal plasticity models. The significant disagreement found between model and experiment in the examples presented above

Figure 11. Contour plot from the FEM code showing the $_{11}$ component of the rotation matrix defining the initial lattice orientations.

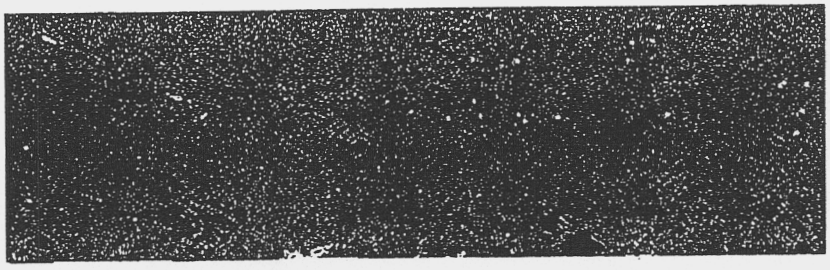

Figure 12. Contours of maximum principal logarithmic strain following 4% strain of the model with orientations defined in Figure 11.

highlights the importance of conducting such validation studies. Validation studies define the expected quality of the predictions and identify aspects of the problem which must be defined accurately to obtain a reasonable solution.

Based on the success of Taylor-like polycrystal models for predicting texture evolution, it was at first anticipated that a discretized model of a two dimensional section would give nearly correct orientation predictions since equilibrium and compatibility could both be satisfied. This proved not to be the case. It was then suggested that properly accounting for the details of the grain structure and the boundary conditions would fix the problem. This was also not sufficient. Even when the full three dimensional grain structure was known and boundary condition approximations were avoided by modeling the full specimen, the model failed to predict gross features of the specimen deformation as well as the significant orientation gradients. There is obviously something else that is not being modeled properly.

The potential causes of the disagreement have not been investigated thoroughly, so additional studies must be conducted to isolate the factors and propose guidelines for future modeling. Possible sources of modeling error can be put into two broad classes: deficiencies in the finite element model and deficiencies in the crystal model itself.

Of several possible finite element model deficiencies, one is clearly inadequate spatial discretization. In the columnar grain studies of Bhattacharyya, et al[27], the element size was larger than 150μm and the element size was on the order of 700μm in the study by Weiland and Becker[26]. In both cases, the experiments showed band formation with a spacing on the order of 100μm. To capture features of this size, the elements would need to be on the order of 10μm or less. It is clear that the models would never capture these features with the given discretization.

Additionally, the alignment of the elements with the direction of the slip gradients may play a role. It has long been known that proper mesh construction is critical in capturing incipient shear bands[42]. If the mesh is not aligned properly, the added mesh constraint can delay or prevent the appearance of a shear band. In the case of crystal modeling, the banded structure observed by Bhattacharyya, et al[27] appeared in some grains and not in others, and the band features observed in Figure 8 were not present in another portion of the same grain, Figure 7. This indicates that these patterns can be excited or suppressed without significant modification to the stress field. Given that the local deformation field might not be difficult to perturb, it is possible that constraints imposed by the spatial discretization may be inhibiting gradients in the deformation field. Consider the orientation gradient shown in Figure 6. This gradient is oblique to the mesh, and it may not be possible for the elements to deform in a manner consistent with the observed orientation gradients. If this were the case, it would also explain the inability of the model to capture the correct sign for the slope on the left side of the specimen.

Deficiencies in the slip system hardening relations used in crystal plasticity models are well known. A constant slip system interaction matrix was assumed. This does not properly account for interactions among slip systems[35]. Although using a more sophisticated slip system interaction model[38] did not improve the predictions in the tricrystal simulations, that does not mean that the slip system model is unimportant. It is just not the dominant reason for the failure of the model in that simulation. It is also known that some crystals do not follow the Schmid law. Slip can depend on pressure as well as stress not acting directly on the slip system of interest[43]. This is generally not a big effect for aluminum, so it is doubtful that omission of non-Schmid contributions had a significant impact on these predictions.

REFERENCES

1. Von M. Polanyi, Rontegenographische bestimmung von kristallanordnungen, *Naturwissenschaften* 10:411 (1922).
2. E. Schmid, *Proc. Int. Cong. Appl. Mech. (Delft)*, 342 (1924).
3. G.I. Taylor and C.F. Elam, The plastic extension and fracture of aluminum crystals, *Proc. R. Soc. London, Sec A* 108:28 (1925).
4. G.I. Taylor, Plastic strain in metals, *J. Inst. Met.* 62:307 (1938).
5. J.F.W. Bishop and R. Hill, A theoretical derivation of the plastic properties of a polycrystalline face centered metal, *Philos. Mag.* 42:414 (1951).
6. J.W. Hutchinson, Plastic deformation of B.C.C. polycrystals, *J. Mech. Phys. Solids* 12:25 (1964).
7. R. Hill and J.R. Rice, Constitutive analysis of elastic-plastic crystals at arbitrary strain, *J. Mech. Phys. Solids* 20:401 (1972).
8. H. Honneff and H. Mecking, *Textures in Metals*, G. Gottstein and K. Lucke, eds., Springer, Berlin (1978).
9. R.J. Asaro, Crystal plasticity, *J. Appl. Mech.* 50:921 (1983).
10. U.F. Kocks, C. Tome and G.R. Canova, Effective-cluster simulation of polycrystal plasticity, in: *Large Deformations of Solids*, J. Gittus, J. Zarka and S. Nemat-Nasser, eds., Elsevier Applied Science, New York (1986).
11. R.J. Asaro, Micromechanics of crystals and polycrystals, in: *Advances in Applied Mechanics*, Academic Press, New York (1983).
12. D. Peirce, R.J. Asaro and A. Needleman, An analysis of nonuniform and localized deformation in ductile single crystals, *Acta Metall.* 30:1087 (1982).
13. D. Peirce, R.J. Asaro and A. Needleman, Material rate dependence and localized deformation in crystalline solids, *Acta Metall.* 31:1951 (1983).
14. S.V. Harren, H.E. Deve and R.J. Asaro, Shear band formation in plane strain compression, *Acta Metall.* 36:2435 (1988).
15. F. Havilcek, J. Kratochvil, M. Tokuda and V. Lev, Finite element model of plastically deformed multicrystal, *Int. J. Plast.* 6:281 (1990).
16. M.A. Zikry and S. Nemat-Nasser, High strain-rate localization and failure of crystalline materials, *J. Mech. Mater.* 10:215 (1990).
17. R. Becker, J.F. Butler, H. Hu and L.A. Lalli, Analysis of an aluminum single crystal with unstable initial orientation (001)[110] in channel die compression, *Metal. Trans. A* 22:45 (1991).
18. S.R. Kalidindi, C.A. Bronkhorst and L. Anand, Crystallographic texture evolution in bulk deformation processing of FCC metals, *J. Mech. Phys. Solids* 40:537 (1992).

This work was performed under the auspices of the U.S. Department of Energy by the University of California, Lawrence Livermore National Laboratory under Contract No. W-7405-Eng-48.

19. A.J. Beaudoin, K.K. Mather, P.R. Dawson, G.C. Johnson, Three dimensional deformation process simulation with explicit use of polycrystalline plasticity models, *Int. J. Plast.* 9:833 (1993).
20. M. Saeedvafa, J.R. Rice, Crack tip fields in a material with three independent slip systems: NiAl single crystal, *Modelling and Simul. Mater. Sci. Engr.* 1:53 (1992).
21. R. Mohan, M. Ortiz and C.F. Shih, Mode mixity effects on crack tip deformation in ductile single crystals, *Acta. Metall. Mater.* 40:1907 (1992).
22. R. Becker, Analysis of texture evolution in channel die compression-I. Effects of grain interaction, *Acta Metall. Mater.* 39:1211 (1991).
23. R. Becker, Effects of strain localization on surface roughening during sheet forming, *Acta Mater.* 46:1385 (1998).
24. A.J. Beaudoin, J.D. Bryant and D.A. Korzekwa, Analysis of ridging in aluminum, *Metall. Trans. A* 29:2323 (1998).
25. R. Becker and S. Panchanadeeswaran, Effects of grain interactions on deformation and local texture in polycrystals, *Acta Metall. Mater.* 43:2701 (1995).
26. H. Weiland and R. Becker, Analysis of mesoscale deformation structures in aluminum, *Deformation induced Microstructures: Analysis and Relation to Properties*, J.B. Bilde-Sørensen, J.V. Cartensen, N. Hansen, D. Juul Jensen, T. Leffers, W. Pantleon, O.B. Pedersen and G. Winther, eds., Risø National Laboratory, Roskilde, Denmark (1999).
27. A. Bhattacharyya, E. El-Danaf, S.R. Kalidindi and R.D. Doherty, Evolution of grain-scale microstructure during large strain simple compression of polycrystalline aluminum with quasi-columnar grains: OIM measurements and numerical simulations, Submitted for publication.
28. F.J. Humphreys, Quantitative metallography by electron backscattered diffraction, *J. Microscopy* 195:170 (1998).
29. S. Vogel, P. Klimanek, D. Juul Jensen, and H. Richter, Effect of texture on the development of grain size distribution during normal grain growth, *Scripta Mater.* 34:1225 (1996).
30. F.J. Humphreys, Modelling microstructural evolution during annealing, Presented at workshop on *Integrated Materials Modelling*, Achen, Germany (1999).
31. B. Radhakrishnan and P. Baggathun, Manuscript in preparation.
32. M. Ortiz, M. and L. Stainier, The variational formulation of viscoplastic constitutive updates, *Comp. Meth. Appl. Mech. Engr.* 171:419 (1999).
33. C. Miehe, Exponential map algorithm for stress updates in anisotropic multiplicative elastoplasticity for single crystals, *Int. J. Num. Meth. Engr.* 39:3367 (1996).
34. S.V. Harren, On the constitutive behavior of thermoelastic-viscoplastic crystals: theoretical and computational issues, Submitted for publication.
35. J.L. Bassani, Single crystal hardening, *Appl. Mech. Rev.* 43:S320 (1990).
36. L. Anand and M. Kothari, A computational procedure for rate-independent crystal plasticity, *J. Mech. Phys. Solids* 44:525 (1996).
37. J.L. Bassani and T.-Y. Wu, Latent hardening in single crystals II. Analytical characterization and predictions, *Proc. Roy. Soc. Lond. A* 435:21 (1991).
38. A.M. Cuitino and M. Ortiz, Computational modelling of single crystals, *Modelling Simul. Mater. Sci. Engr.* 1:225 (1992).
39. S. Panchanadeeswaran, R.D. Doherty and R. Becker, Direct observation of orientation change by channel die compression of polycrystalline aluminum--use of a split sample, *Acta Mater.* 44:1233 (1996).
40. J.S. Stolken, W.E. King, A.J. Schwartz, M.A. Wall, and L. Nguyen, Reconstruction of a 3D microstructure using orientation imaging microscopy, in: *Advances in Materials Problem Solving with the Electron Microscope*, C. Allen, J. Bentley, U. Dahmen and I. Petrov, eds., MRS Proceedings, Boston (1999).
41. J.A. Kallivayalil, H. Weiland and R. Becker, Unpublished research.
42. V. Tvergaard, A. Needleman and K.K. Lo, Flow localization in the plane strain tensile test, *J. Mech. Phys. Solids* 29:115 (1981).
43. Q. Qin and J.L. Bassani, Non-Schmid yield behavior in single crystals, *J. Mech. Phys. Solids* 40:813 (1992).